IOP Publishing J. Phys. B: At. Mol. Opt. Phys. 59 (2026) 175601 https://doi.org/10.1088/1361-6455/aea044

Journal of Physics B: Atomic, Molecular and Optical Physics

RECEIVED
9 June 2026

REVISED
11 August 2026

ACCEPTED FOR PUBLICATION
28 August 2026

PUBLISHED
8 September 2026

PAPER

Electron recollision with bright squeezed vacuum light

Haoyu Liu[1], **Jianmin Yuan**[1,2,*] **and Xu Wang**[1,*]

[1] Graduate School, China Academy of Engineering Physics, Beijing 100193, People's Republic of China
[2] Institute of Atomic and Molecular Physics, Jilin University, Changchun 130012, People's Republic of China
[*] Authors to whom any correspondence should be addressed.

E-mail: jmyuan@gscaep.ac.cn and xwang@gscaep.ac.cn

Keywords: recollision, bright squeezed vacuum light, virtual detector method

Abstract

Electron recollision is a cornerstone of strong-field physics driven by coherent (classical) light, yet its applicability beyond coherent light remains largely unexplored. A particularly intriguing case is bright squeezed vacuum (BSV), a macroscopic quantum state of light characterized by large intensity fluctuations and a vanishing mean electric field. While BSV has recently been shown to induce nonperturbative strong-field phenomena, whether it can support the coordinated electron return dynamics that underpin the recollision framework is unknown. Here, employing a virtual detector (VD) method, we investigate recollision dynamics from both local and global perspectives by extracting probability currents and velocity distributions of the returning electron wave packet and by reconstructing probability-flow trajectories under coherent and BSV excitation. For coherent light, the VD analysis reproduces the conventional recollision results. In contrast, BSV-driven dynamics exhibit a compressed velocity distribution of the returning electron current and strongly dispersed probability-flow trajectories, revealing substantial modifications of recollision dynamics induced by the quantum nature of the driving field.

1. Introduction

In strong-field atomic physics, laser-driven electron recollision [1–3] is a key process underlying a wide range of phenomena, including high-order harmonic generation (HHG) and attosecond pulse production [4–7], nonsequential double ionization [8–12], laser-induced electron diffraction [13–15], laser-assisted nuclear excitation [16, 17], etc. In a strong laser field, an electron is first released through tunneling ionization, forming a continuum wave packet. The laser field then drives the electron away from the parent ion, accelerates it in the continuum, and can subsequently reverse its motion, causing it to revisit the ion core. The remarkable explanatory power of the recollision framework relies on two essential ingredients: the generation of a spatially localized electron wave packet upon ionization and the coherence of the driving field, which enables synchronized, quasi-classical electron trajectories and well-defined return dynamics.

Recently, the initiation of the above-mentioned strong-field phenomena has been extended beyond coherent light. In particular, bright squeezed vacuum (BSV) light—a macroscopic quantum state of light characterized by large fluctuations and a vanishing mean electric field [18–20]—has been experimentally shown to drive nonperturbative harmonic generation [21], sideband formation [22, 23], multiphoton ionization [24, 25], and tunneling ionization [26]. Theoretically, BSV light–matter interactions have been investigated in several strong-field contexts, including HHG [27–30], atomic ionization [31–33], and Compton scattering [34]. A commonly adopted approach employs the Husimi distribution to represent BSV-driven dynamics as a superposition of coherent-state (classical-field) responses [35–37]. Previous work has also shown that the temporal evolution of the electron-wavepacket width under BSV light exhibits features reminiscent of recollision dynamics [38]. In addition, Husimi-distribution-based averaging over classical-field responses has been used to examine whether the returning electron can exceed the recollision-energy threshold required for nonsequential double ionization under BSV driving [33].

However, a direct fully quantum dynamical characterization of how BSV light modifies electron recollision is still lacking. Such a characterization is essential for assessing whether the conventional recollision picture, and in particular its interpretation of strong-field emission processes such as HHG in terms of returning-electron dynamics, remains applicable beyond coherent (classical) light.

To address this issue, a more direct characterization of electron motion within the fully quantum coupled light–atom dynamics is required. Although the strongly fluctuating nature of BSV light renders deterministic trajectory descriptions based on a classical driving field problematic, the evolution of the electron probability density remains well defined. We therefore employ the virtual detector (VD) method [39–44] to record returning probability currents and reconstruct the global flow of the electron wave packet. The resulting trajectories are derived from the probability-current field, enabling the electron dynamics to be reformulated within a quantum-hydrodynamic framework [45]. These trajectories are closely related to Bohmian trajectories [46–48] and provide an intuitive visualization of the evolution of the electron probability flow [49–51]. The VD method has previously been employed to extract momentum distributions from early-stage wavefunction evolution with reduced computational cost [39, 40] and to investigate tunneling ionization dynamics [52–54].

In this work, we investigate electron dynamics driven by BSV light using the VD method to analyze electron probability currents. We first derive the continuity equation and the corresponding electron current velocity in a quantum-field-driven atomic system. By numerically solving the coupled light–atom Schrödinger equation and extracting local current velocities near the parent ion core, we obtain the velocity distribution of the returning probability current. For coherent light, the extracted distribution agrees closely with the recollision velocities predicted by the classical model. In contrast, under BSV light, the return-velocity distribution becomes substantially compressed. To uncover the dynamical origin of this behavior, we extend the VD analysis to the entire simulation domain and reconstruct global probability-flow trajectories from the velocity field. These trajectories reveal how the electron motion is modified under BSV driving and provide a direct dynamical interpretation of the compressed return-velocity distribution. Together, our results offer a direct assessment of the applicability of the recollision picture in the regime of quantum-light-driven strong-field dynamics.

The remainder of this article is organized as follows. In section 2, we introduce the theoretical framework for quantum light–atom interactions and the VD method. Section 3 presents the main results, including returning-current velocity distributions, reconstructed probability-flow trajectories, phase-space analyses, and spectral features under coherent and BSV light. Further remarks are provided in section 4, and conclusions are given in section 5.

2. Methods

2.1. Quantum light–atom interaction

The Hamiltonian of the coupled single-mode light and atom system is $\hat{H} = \hat{H}_\mathrm{A} + \hat{H}_\mathrm{L} + f(t)\hat{H}_\mathrm{int}$, where $\hat{H}_\mathrm{A}$ is the atomic Hamiltonian and $\hat{H}_\mathrm{L} = \omega\hat{a}^\dagger\hat{a}$ describes the quantized electromagnetic field, with ω the angular frequency of the driving field. Assuming that the field polarization is aligned with the atomic dipole, the interaction Hamiltonian is written as $\hat{H}_\mathrm{int} = -\hat{\mathrm{d}}\hat{E}$, where $\hat{d}$ is the dipole operator, $\hat{E} = \mathrm{i}\epsilon^{(1)}(\hat{a} - \hat{a}^\dagger)$ is the electric-field operator, and $f(t)$ is the trapezoidal pulse envelope used in the numerical propagation, consisting of a 4-cycle turn-on, a 7-cycle plateau, and a 4-cycle turn-off. Here, $\epsilon^{(1)} = \sqrt{\omega/2\epsilon_0 V}$ denotes the single-photon field amplitude, with V the quantization volume and ϵ_0 the vacuum permittivity. We model the atom using a one-dimensional soft-core potential [55, 56]: $\hat{H}_\mathrm{A} = \hat{p}_x^2/2 - 1/\sqrt{\hat{x}^2 + \nu^2}$, where $\hat{x}$ and $\hat{p}_x$ are the electron position and momentum operators. The soft-core parameter is chosen as $\nu^2 = 0.67$, giving a ground-state energy of -0.79 atomic units (a.u.), close to the ionization potential of the Ne atom. The one-dimensional soft-core model used here should be regarded as a minimal model that balances computational feasibility with the essential recollision dynamics in the fully quantum light–atom framework. This reduction is suitable for testing the dynamical part of the conventional recollision picture, since the standard return-energy scaling in the classical recollision model is obtained from one-dimensional electron motion along the laser polarization direction [3]. The state evolves as

$$|\Psi(t)\rangle = \hat{T}\exp\left[-\mathrm{i}\int_0^t \left(\hat{H}_\mathrm{A} + \hat{H}_\mathrm{L} + f(t')\hat{H}_\mathrm{int}\right)\mathrm{d}t'\right]|\Psi(0)\rangle, \tag{1}$$

where $\hat{T}$ denotes the time-ordering operator. The initial state is chosen as $|\Psi(0)\rangle = |g, \phi\rangle$, where $|g\rangle$ is the atomic ground state and $|\phi\rangle$ is the quantum state of the driving field. At time t, the system can equivalently be described by the density operator $\hat{\rho}(t) = |\Psi(t)\rangle\langle\Psi(t)|$.

Introducing the canonical light-field quadrature operators [57, 58], $\hat{q} = (\hat{a}^\dagger + \hat{a})/\sqrt{2\omega}$ and $\hat{p}_q = \mathrm{i}\sqrt{\omega/2}(\hat{a}^\dagger - \hat{a})$, the Hamiltonian $\hat{H}$ becomes

$$\hat{H} = \hat{H}_\mathrm{A} + \hat{p}_q^2/2 + \omega^2\hat{q}^2/2 + f(t)\sqrt{2/\omega}\epsilon^{(1)}\hat{d}\hat{p}_q. \tag{2}$$

The state $|\Psi(t)\rangle$ can then be projected onto the joint coordinate representation defined by $\hat{x}|x\rangle = x|x\rangle$ and $\hat{q}|q\rangle = q|q\rangle$, and expressed as

$$\begin{aligned}\Psi(x,q,t) &= \langle x,q|\Psi(t)\rangle \\ &= \int \mathrm{d}x'\mathrm{d}q'\langle x,q|\mathrm{e}^{-\mathrm{i}\hat{H}t}|x',q'\rangle\langle x',q'|\Psi(0)\rangle \\ &= \hat{T}\exp\left[-\mathrm{i}\int_0^t\left(H_\mathrm{A} - \partial_q^2/2 + \omega^2q^2/2 - \mathrm{i}f(t')\sqrt{2/\omega}\epsilon^{(1)}\mathrm{d}\partial_q\right)\mathrm{d}t'\right]\Psi(x,q,0),\end{aligned} \tag{3}$$

where ∂_q denotes differentiation with respect to the light-field quadrature coordinate q, $d = -x$, and $H_\mathrm{A} = -\partial_x^2/2 - 1/\sqrt{x^2+\nu^2}$. To characterize the electron dynamics, we consider the reduced density matrix of the atomic subsystem in the electron position representation, obtained by tracing out the light-field degrees of freedom [59]

$$\begin{aligned}\rho_\mathrm{A}(x,x',t) &= \langle x|\mathrm{Tr}_\mathrm{L}[\hat{\rho}(t)]|x'\rangle \\ &= \sum_n\iint \mathrm{d}q\mathrm{d}q'\langle n|q\rangle\langle x,q|\Psi(t)\rangle\langle\Psi(t)|x',q'\rangle\langle q'|n\rangle \\ &= \sum_n\iint \mathrm{d}q\mathrm{d}q'\Psi(x,q,t)\Psi^*(x',q',t)\phi_n(q')\phi_n^*(q) \\ &= \iint \mathrm{d}q\mathrm{d}q'\Psi(x,q,t)\Psi^*(x',q',t)\langle q'|q\rangle \\ &= \int \mathrm{d}q\Psi(x,q,t)\Psi^*(x',q,t),\end{aligned} \tag{4}$$

where $\phi_n(q) \equiv \langle q|n\rangle$. The diagonal elements of the reduced density matrix give the electron probability density in position space, $\rho_\mathrm{A}(x,t) \equiv \rho_\mathrm{A}(x,x,t)$.

2.2. Probability current of the electron and the VD method

To describe the dynamics of the electron density, we derive the continuity equation for the reduced atomic system and identify the corresponding probability current. This allows us to define the local current velocity, which forms the basis of the VD method used in this work.

Starting from the Liouville equation for the density matrix [60–62], we obtain

$$\begin{aligned}\frac{\partial}{\partial t}\rho_\mathrm{A}(x,x',t) &= -\mathrm{i}\langle x|\mathrm{Tr}_\mathrm{L}\left[\hat{H},\hat{\rho}(t)\right]|x'\rangle \\ &= -\mathrm{i}\langle x|\left[\mathrm{Tr}_\mathrm{L}\left(\hat{H}_\mathrm{L}\hat{\rho}(t)\right) - \mathrm{Tr}_\mathrm{L}\left(\hat{\rho}(t)\hat{H}_\mathrm{L}\right)\right]|x'\rangle \\ &\quad -\mathrm{i}\left[-\frac{1}{2}\left(\partial_x^2 - \partial_{x'}^2\right) + \left(V(x) - V(x')\right)\right]\rho_\mathrm{A}(x,x',t) \\ &\quad -f(t)(d-d')\mathcal{A}(x,x',t),\end{aligned} \tag{5}$$

where $\mathcal{A}(x,x',t)$ is defined by

$$\begin{aligned}\mathcal{A}(x,x',t) &\equiv \epsilon^{(1)}\sum_{n,m}\langle n|\left(\hat{a} - \hat{a}^\dagger\right)|m\rangle\langle x|\hat{\rho}_{nm}(t)|x'\rangle \\ &= \epsilon^{(1)}\sum_{n=0}^{\infty}\sqrt{n+1}\left(\rho_{n,n+1}(x,x',t) - \rho_{n+1,n}(x,x',t)\right).\end{aligned} \tag{6}$$

Since $\hat{H}_\mathrm{L}$ acts only on the light-field degrees of freedom, the cyclic property of the trace gives $\mathrm{Tr}_\mathrm{L}(\hat{H}_\mathrm{L}\hat{\rho}(t)) = \mathrm{Tr}_\mathrm{L}(\hat{\rho}(t)\hat{H}_\mathrm{L})$, so the contribution from $\hat{H}_\mathrm{L}$ vanishes. In the diagonal limit $x' \to x$, the atomic-potential term vanishes because $V(x) - V(x') \to 0$, and the interaction term also vanishes because

$f(t)(d-d') \to 0$. Taking this limit, we obtain the continuity equation for the electron probability density [51, 63]

$$\begin{aligned}\frac{\partial}{\partial t}\rho_{\mathrm{A}}(x,t) &= \frac{\mathrm{i}}{2}\lim_{x'\to x}\left(\partial_x^2-\partial_{x'}^2\right)\rho_{\mathrm{A}}(x,x',t)\\ &= \frac{\mathrm{i}}{2}\lim_{x'\to x}\left(\partial_x+\partial_{x'}\right)\left(\partial_x-\partial_{x'}\right)\rho_{\mathrm{A}}(x,x',t)\\ &= \lim_{r\to 0}\partial_R\left(\mathrm{i}\partial_r\rho_{\mathrm{A}}(R,r,t)\right)\\ &= -\partial_x j(x,t),\end{aligned} \tag{7}$$

where the center coordinate and relative coordinate are defined as $R=(x+x')/2$ and $r=x-x'$, respectively, with $\partial_x+\partial_{x'}=\partial_R$ and $\partial_x-\partial_{x'}=2\partial_r$. The probability current is therefore identified from the continuity equation as

$$j(x,t) = -\frac{\mathrm{i}}{2}\lim_{x'\to x}\left(\partial_x-\partial_{x'}\right)\rho_{\mathrm{A}}(x,x',t), \tag{8}$$

which is equivalent to the expectation value of the current-density operator $\hat{j}(x)$ [64, 65]

$$j(x,t) = \mathrm{Tr}\left[\hat{\rho}_{\mathrm{A}}(t)\hat{j}(x)\right], \tag{9}$$

with

$$\hat{j}(x) = \frac{1}{2}\left(|x\rangle\langle x|\hat{p}_x+\hat{p}_x|x\rangle\langle x|\right). \tag{10}$$

The local velocity associated with the probability current is then

$$v(x,t) = \frac{j(x,t)}{\rho_{\mathrm{A}}(x,t)}. \tag{11}$$

The local probability current and velocity field can be accessed by introducing VDs at selected positions in space. At a detector position x_{d}, the VD records the time-dependent current $j(x_{\mathrm{d}},t)$, thereby resolving the local returning current near the parent nucleus [33, 42]. The corresponding local current velocity is $v(x_{\mathrm{d}},t)=j(x_{\mathrm{d}},t)/\rho_{\mathrm{A}}(x_{\mathrm{d}},t)$. Figure 1(a) schematically illustrates the VD method. As the initial electron wave packet evolves under the driving field, a detector at a fixed position records the local probability current, from which the corresponding flow velocity is determined. Because the VD method extracts time-dependent dynamical information from the electron probability density and current without altering the state evolution, and does not require a well-defined mean electric-field waveform, it can be implemented within the present fully quantum light–atom framework and is suitable for comparing coherent- and BSV-driven recollision dynamics on the same footing.

In the present work, the VD method is primarily used to investigate recollision dynamics under BSV light, with coherent light considered for comparison. The two cases are compared at the same field intensity, defined as $I=c\omega NV^{-1}=\epsilon_0 c|E|^2/2$ [57], where c is the speed of light and N is the mean photon number. The corresponding effective electric-field amplitude is $|E|=\sqrt{2\omega N/(\epsilon_0 V)}$. Under this intensity matching, the ponderomotive energy in both cases is determined by $U_{\mathrm{p}}=|E|^2/4\omega^2$ [38]. In the present calculations, the mean photon number is fixed at $N=10^4$. The full system wavefunction $\Psi(x,q,t)$ in equation (3) is obtained by numerically propagating the coupled light–atom system in the joint electron-field coordinate representation (x,q). For the electronic coordinate, the simulation box ranges from $x_{\mathrm{min}}=-120$ a.u. to $x_{\mathrm{max}}=120$ a.u., with a grid spacing of $\mathrm{d}x=0.1$ a.u. For the light-field quadrature coordinate, the numerical domain extends from $q_{\mathrm{min}}=-1790$ a.u. to $q_{\mathrm{max}}=1790$ a.u., with a grid spacing of $\mathrm{d}q=0.03$ a.u. Similar numerical approaches based on fixing the mean photon number have previously been employed in [66, 67].

3. Results and discussion

In this section, we employ the VD method to compare electron dynamics driven by coherent and BSV light. We first extract the local velocity distributions of the returning electron current as a function of the ponderomotive energy U_{p}, and subsequently reconstruct the global probability-flow trajectories from the velocity field $v(x,t)$. These complementary local and global observables provide a direct visualization of the underlying electron dynamics, revealing how recollision processes driven by BSV light differ from the classical-like behavior observed under coherent light.

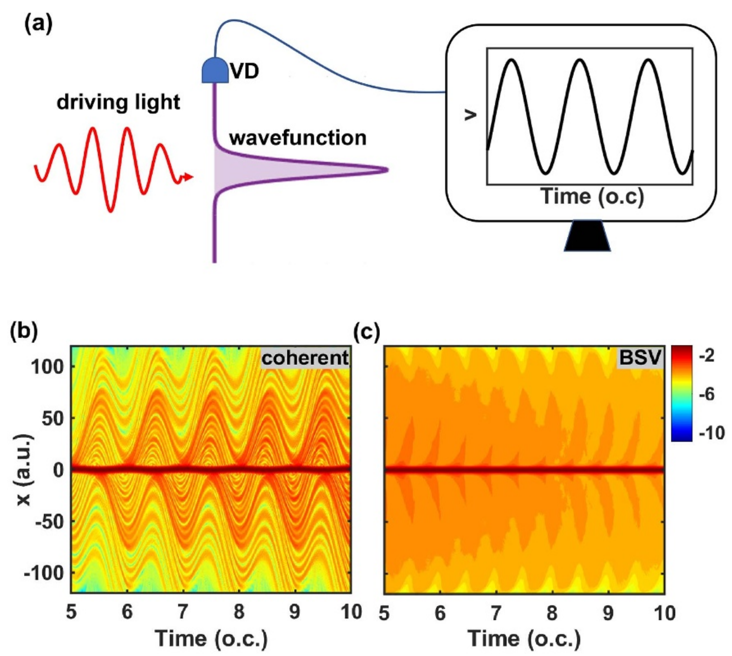

Figure 1. (a) Schematic illustration of the one-dimensional VD method. (b), (c) Temporal evolution of the electron probability density in position space under coherent and BSV light, respectively, for a wavelength of 800 nm and an average intensity of 3×10^{14} W cm^{-2}. The total pulse duration is 15 optical cycles (o.c.). The color scale in (b), (c) represents $\log_{10}[\rho_A(x,t)]$.

3.1. Local velocity distribution of the returning electron

Figures 1(b) and (c) display the time evolution of the electron probability density, $\rho_A(x,t)$, in position space under coherent and BSV light at an average intensity of 3×10^{14} W cm^{-2}. For coherent light, pronounced interference fringes emerge and the probability density exhibits regular oscillations driven by the coherent mean electric field. In contrast, under BSV light, the interference pattern becomes significantly less distinct owing to the strong field fluctuations. Despite the absence of a coherent mean field, the probability density still undergoes pronounced temporal oscillations, with a dominant frequency approximately twice that of the optical carrier frequency. This factor of two originates from the BSV electric-field variance, the fluctuation pattern of which repeats after half an optical cycle.

Based on these time-dependent density distributions, a VD placed at the boundary between the bound and unbound regions is used to extract the local velocity of the returning electron current at position x_d. For a detector on the negative-x side ($x_d < 0$), the ionic core lies to the right of the detector, so a positive current corresponds to probability flow toward the core. Therefore, only time samples satisfying $j(x_d,t) > 0$, or equivalently $v(x_d,t) > 0$, are included in the returning-current velocity distribution for the negative-x VD used below. For a detector on the positive-x side, the sign criterion is reversed. At each retained instant, the local velocity $v(x_d,t)$ is assigned a weight $P(t) = |j(x_d,t)|$, corresponding to the magnitude of the instantaneous returning probability current. Throughout the laser pulse, the time-dependent velocities $v(x_d,t)$ are sampled and binned into intervals $I_i = [v_i, v_i + \mathrm{d}v)$. For each interval, the weights associated with all times satisfying $v(x_d,t) \in I_i$ are accumulated and subsequently normalized, yielding the velocity distribution $P(v_i) = \sum_{v(t)\in I_i} P(t)/Z$ where $Z = \sum_t P(t)$ is the normalization factor. In the limit of sufficiently small dv, $P(v)$ may be interpreted as the probability density of the returning velocity and satisfies the normalization condition $\int P(v)\,\mathrm{d}v = 1$ [68].

Figure 2 presents the velocity distribution of the returning electron current measured by a VD located at $x_d = -10$ a.u. as a function of the ponderomotive energy U_p for both coherent and BSV light. The dashed line indicates the return velocity corresponding to the maximum recollision energy of $3.17U_p$, as predicted by the classical recollision model in the absence of the ion-core Coulomb potential. As will be demonstrated below through phase-space analyses and additional calculations with different VD positions, moderate changes in the detector location do not qualitatively affect the extracted velocity distributions.

Under coherent light, the distribution spans a broad velocity range, and the upper edge of the populated velocity distribution at each U_p lies close to the $3.17U_p$ boundary. This indicates that the maximum return velocity grows with U_p following the usual $\sim\sqrt{U_p}$ scaling [3]. Under BSV light, by contrast, the distribution remains largely confined to a narrow low-velocity strip ($v < 0.25$ a.u.) over the

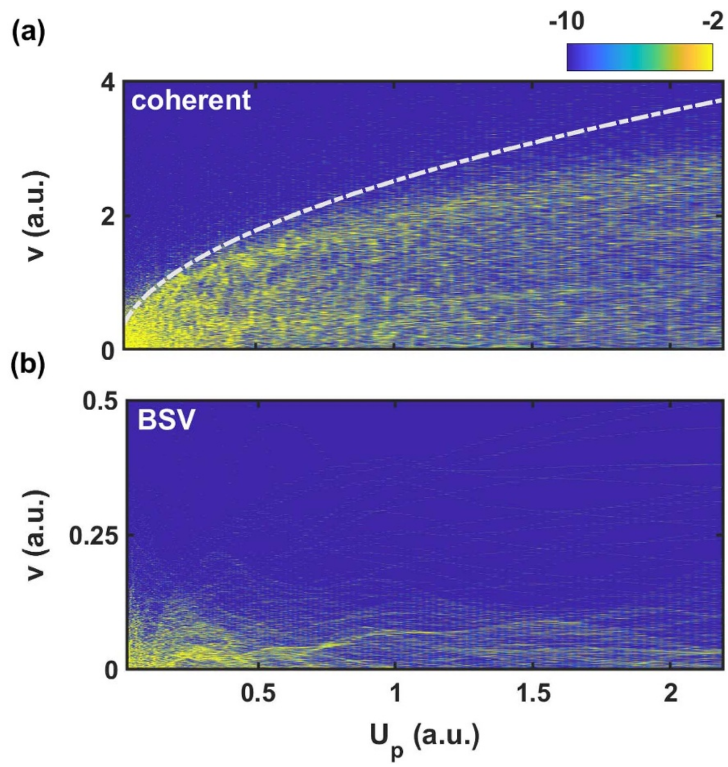

Figure 2. Velocity distributions of the returning electron current recorded at $x_d = -10$ a.u. using the VD method under (a) coherent and (b) BSV light, as functions of the ponderomotive energy U_p. The dashed line indicates the velocity corresponding to the maximum return energy $3.17U_p$ predicted by the classical recollision model. The color scale represents $\log_{10}[P(v, U_p)]$.

entire U_p range. Although the maximum return velocity increases slightly with U_p, the probability weight in this higher-velocity region remains weak. The maximum return velocity under BSV light also stays below 0.5 a.u., substantially lower than in the coherent case.

The close agreement between the VD-extracted upper velocity boundary in figure 2(a) and the well-established classical prediction demonstrates that the local return-velocity analysis faithfully captures the standard recollision dynamics under coherent light. Because the same return energy determines the conventional HHG cutoff, $3.17U_p + I_p$ [3], the familiar correspondence between the maximum returning-electron velocity and the harmonic cutoff remains valid within the present quantum model.

The situation is qualitatively different under BSV light. Although the returning-current velocity is substantially lower than in the coherent case and exhibits only a weak dependence on U_p, previous studies have shown that the BSV-driven HHG spectrum broadens markedly with increasing U_p [27]. Furthermore, for the same U_p, BSV light can generate HHG spectra that are both broader and more intense than those produced by coherent light [29]. These observations indicate that, under BSV light, the returning-current velocity is no longer directly correlated with either the spectral extent or the intensity of the emitted harmonics. Consequently, the conventional link between high-velocity electron recollision and high-frequency radiation breaks down, pointing to a fundamentally different mechanism underlying BSV-driven HHG. Such a mechanism can be described within the same fully quantum light–atom coupling framework, as shown in our previous treatment of BSV-driven HHG based on fluctuation correlations of the dipole operator rather than on the conventional induced-dipole response [30].

3.2. Global velocity field and electron trajectories

We next characterize the evolution of the electron probability flow by distributing VDs throughout the full simulation domain and obtaining the velocity field $v(x,t)$. This allows us to examine whether a dynamical process analogous to classical recollision can be identified under BSV light. Based on the ground-state wave function of the one-dimensional model atom, we compute the cumulative distribution function of the probability density and generate initial electron positions using inverse transform sampling [69, 70]. The recorded velocity field $v(x,t)$ is then used to numerically integrate the equation of motion $\mathrm{d}x/\mathrm{d}t = v(x,t)$ [51, 63], thereby reconstructing probability-flow trajectories. Since $v(x,t)$ assigns a unique velocity to each position at a given time, these trajectories do not cross [48].

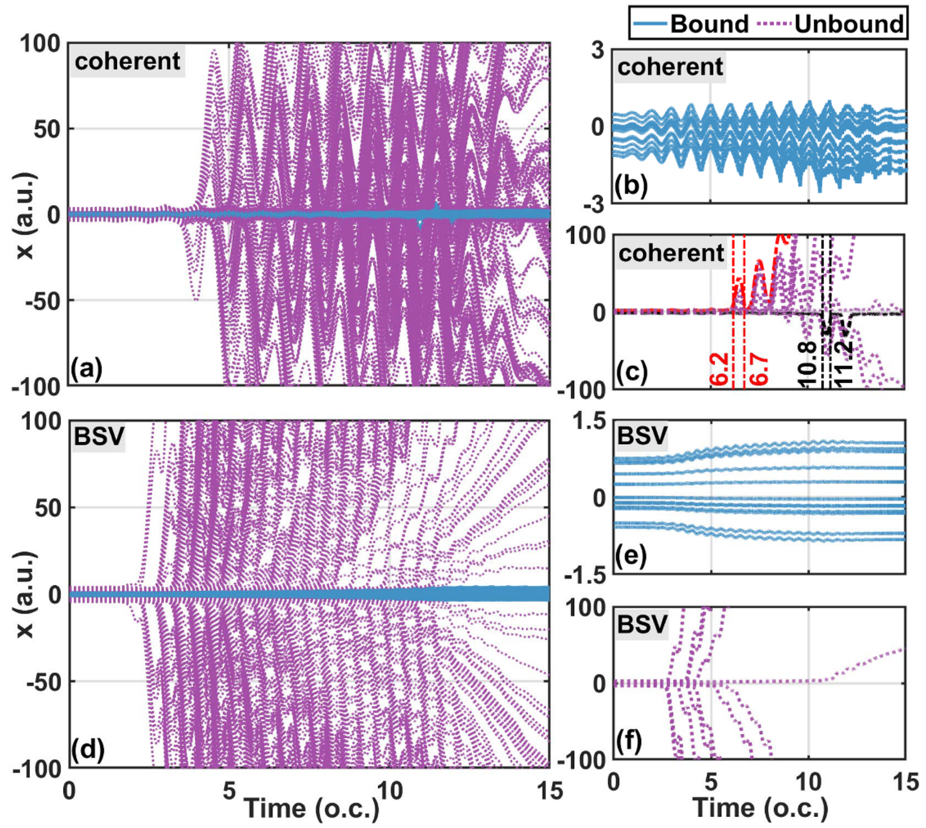

Figure 3. Trajectories reconstructed from the global velocity field $v(x,t)$ with initial positions sampled from the atomic ground-state wave function. (a) and (d) show 5000 trajectories under coherent and BSV light, respectively. Trajectories satisfying $|x| \leqslant 10$ a.u. throughout the evolution are classified as bound-electron trajectories, while the others are classified as unbound-electron trajectories. (b) and (c) show detailed views of 12 selected bound- and unbound-electron trajectories under coherent light. In (c), the highlighted black and red trajectories illustrate representative closed and semi-closed return structures, respectively, and the vertical dash-dot lines mark their departure and return times. (e) and (f) show the corresponding results under BSV light. The average light intensity is 3×10^{14} W cm^{-2}.

Figure 3 shows the trajectories reconstructed under coherent and BSV light. For each driving field, 5000 trajectories are reconstructed from initial positions sampled according to the ground-state probability density. Increasing the number of sampled trajectories does not qualitatively change the reconstructed pattern. Trajectories that satisfy $|x| \leqslant 10$ a.u. throughout the evolution are classified as bound-electron trajectories, whereas the rest are classified as unbound-electron trajectories. In practice, although the threshold is set at $|x| \leqslant 10$ a.u., the bound-electron trajectories remain almost entirely confined within the narrower range $|x| \leqslant 5$ a.u. under both driving fields.

Under coherent light, the trajectories exhibit a highly ordered oscillatory pattern driven by the mean electric field, as shown in figures 3(a)–(c). The bound-electron trajectories remain concentrated near the atomic nucleus and display only small-amplitude oscillations, as shown in figure 3(b). By contrast, the unbound-electron trajectories undergo large-amplitude excursions. Because of the noncrossing property of the flow, trajectories in the regions $x > 0$ a.u. and $x < 0$ a.u. evolve separately while forming an overall ordered oscillatory structure. Some unbound-electron trajectories first move away from the nucleus and are then pulled back when the field reverses, forming closed or semi-closed return structures, as shown in figure 3(c). For clarity, we further highlight one representative closed trajectory in black and one representative semi-closed trajectory in red among the selected trajectories, and mark their first departure and return times by vertical dash-dot lines. In closed structures, the electron flow remains near the nucleus after the pulse, whereas in semi-closed structures it is driven away again after recollision and does not return to the nucleus by the end of the pulse. This behavior is consistent with the ionization–acceleration–recollision process in the classical recollision model.

Under BSV light, however, the trajectory pattern becomes much more dispersed, as shown in figures 3(d)–(f). The electron flow no longer exhibits a unified direction or coordinated return motion; instead, the flow on both sides tends to diverge outward. Although the bound-electron trajectories remain concentrated near the nucleus, their motion no longer shows the regular mean-field-driven oscillations seen under coherent light, but instead exhibits oscillations accompanied by a directional drift, as

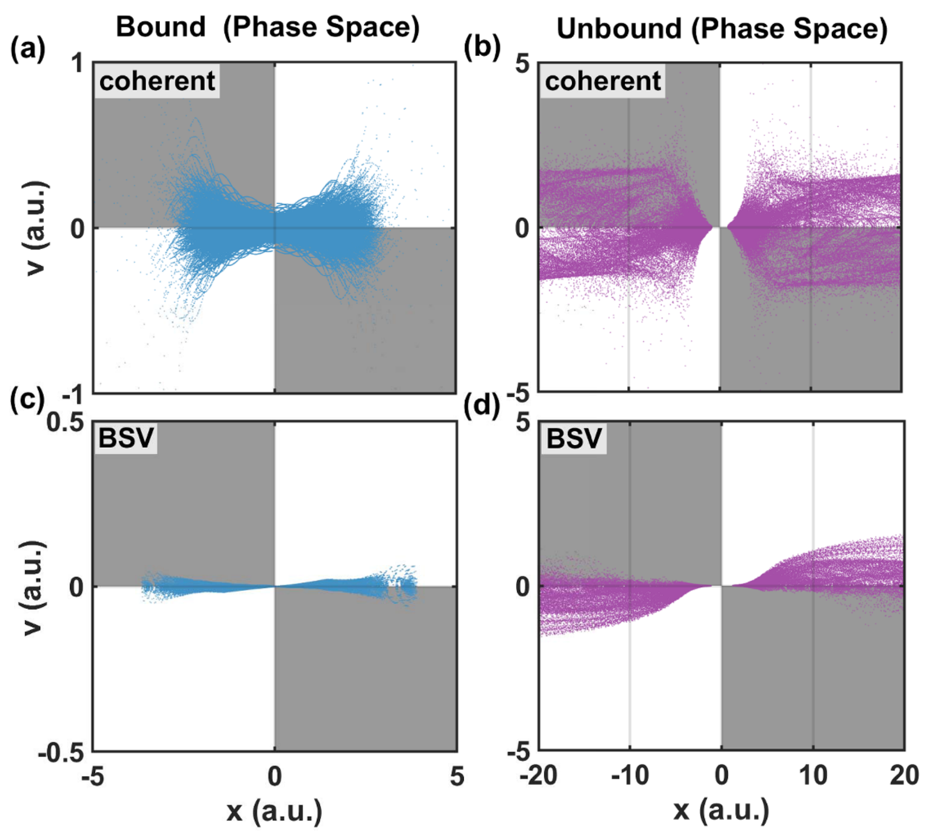

Figure 4. Velocity-position phase-space distributions accumulated over the pulse duration for coherent light [(a), (b)] and BSV light [(c), (d)]. Panels (a) and (c) correspond to bound-electron trajectories, while panels (b) and (d) show unbound-electron trajectories. The shaded regions denote possible returning-current domains, where the velocity and position have opposite signs ($vx < 0$).

shown in figure 3(e). For the unbound-electron trajectories, the distribution remains roughly symmetric with respect to $x = 0$, but the oscillations are no longer organized into a coherent return pattern. Many trajectories show only a brief return tendency and fail to develop into well-defined recollision structures, as shown in figure 3(f).

Figure 4 presents the velocity-position phase-space distributions of the bound and unbound electron trajectories accumulated over the entire pulse duration, providing a direct visualization of the spatially resolved velocity structure of the electron flow. The shaded regions denote the possible returning-current domains, where the velocity and position have opposite signs. Under coherent light, the phase-space distribution of the bound-electron trajectories exhibits a symmetric butterfly-like pattern, as shown in figure 4(a). Both the spatial extent and the velocity range are nearly symmetric with respect to $x = 0$ and $v = 0$, consistent with the regular, near-nucleus oscillatory motion observed in the reconstructed trajectories. For the unbound-electron trajectories (figure 4(b)), the positive and negative velocity boundaries in the region $|x| > 5$ a.u. depend only weakly on position, and the outgoing and returning currents attain comparable velocity limits. Such a phase-space structure arises from a well-organized back-and-forth motion, in which outgoing and returning flows remain coordinated.

In contrast, the phase-space distributions under BSV light differ qualitatively from those obtained under coherent light. As shown in figure 4(c), the bound-electron distribution is strongly compressed along the velocity axis and remains narrowly localized around $v \approx 0$ a.u., exhibiting only a slight asymmetry with respect to $v = 0$. Even more striking is the behavior of the unbound-electron trajectories (figure 4(d)), which display a pronounced asymmetry between the outgoing and returning components. While the outgoing current broadens substantially in velocity as $|x|$ increases, the returning current, highlighted by the shaded region, remains concentrated within a narrow low-velocity band near $v \approx 0$ a.u., with only a weak extension toward larger velocities at large $|x|$. This phase-space structure indicates a strongly unbalanced flow dynamics, where substantial outward spreading is not accompanied by a correspondingly energetic returning current.

Moreover, for both driving fields, the bound-electron trajectories are mainly confined to the near-nucleus region $|x| < 5$ a.u., while some unbound trajectories also remain near the nucleus for several

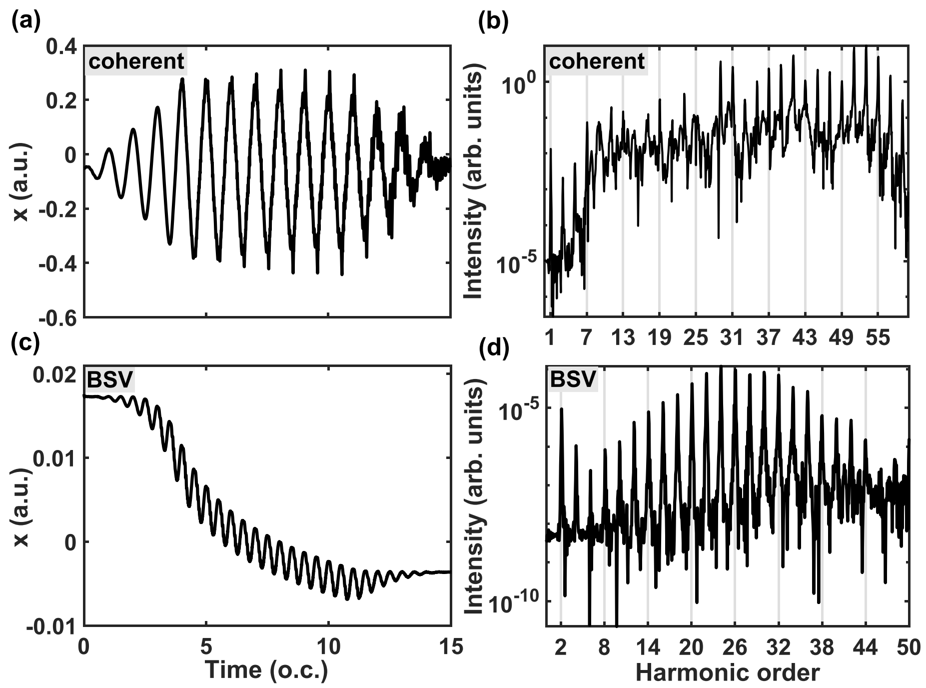

Figure 5. Temporal evolution and Fourier spectra of representative bound-electron trajectories. (a) and (b) correspond to coherent light, while (c) and (d) correspond to BSV light. The vertical scale in the spectral panels (b) and (d) denotes the Fourier-transform intensity of the selected representative trajectory.

cycles. This accounts for the similarity between the near-nucleus phase-space distributions of bound and unbound trajectories. The returning-current velocity characteristics are nearly identical on the $x > 0$ and $x < 0$ sides, showing that the extracted local velocity distribution is insensitive to the detection side. The spatial evolution of the returning-current velocity further provides a basis for the VD-position check discussed in section 4.

Taken together, the trajectory and phase-space analyses reveal two qualitatively different dynamical pictures. Under coherent light, the probability flow retains a clear quantum–classical correspondence with the classical recollision picture, as the reconstructed trajectories and phase-space distributions are associated with organized oscillatory motion and coordinated return behavior. Under BSV light, this correspondence breaks down, as the probability flow becomes dispersed and desynchronized rather than forming a coherent recollision pattern. This dynamical contrast is further reflected in the spectra of representative bound-electron trajectories.

Figure 5 further examines the temporal evolution and Fourier spectra of representative bound-electron trajectories. Previous studies have shown that, under coherent light, the spectrum of a single bound-electron trajectory can capture the main features of the HHG spectrum [71–73]. Consistently, the coherent-light trajectory in figure 5(a) yields a spectrum with a clear sequence of odd harmonics and a plateau structure, as shown in figure 5(b). Under BSV light, however, the situation is qualitatively different. As shown in figure 5(c), the bound-electron trajectory exhibits oscillatory dynamics at approximately twice the carrier frequency. Correspondingly, the Fourier spectrum in figure 5(d) develops pronounced peaks at even harmonic orders. This behavior contrasts with the full HHG spectrum under BSV light, which remains dominated by odd harmonics [27, 28]. This mismatch indicates that, unlike in coherent light, the BSV-driven HHG response is unlikely to be captured by a single representative trajectory or by directly linking the trajectory spectrum to the HHG spectrum.

4. Further remarks

The first remark concerns the choice of the VD position. In figure 2, the velocity distribution of the returning electron current is extracted at $x_\mathrm{d} = -10$ a.u., close to the boundary between the bound and unbound regions. To assess the sensitivity of the results to the detector location, we repeat the analysis at $x_\mathrm{d} = -20$ a.u., as shown in figure 6. The main features remain unchanged: under coherent light, the

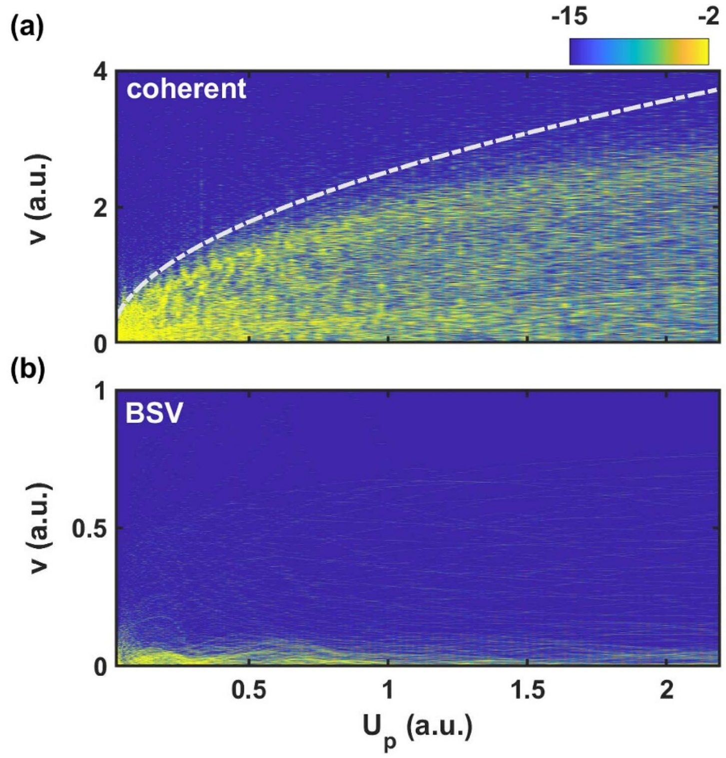

Figure 6. Velocity distributions of the returning electron current recorded at $x_d = -20$ a.u. using the VD method under (a) coherent and (b) BSV light, as functions of the ponderomotive energy U_p. The dashed line indicates the velocity corresponding to the maximum return energy $3.17U_p$ predicted by the classical recollision model.

velocity distribution broadens with increasing U_p and closely follows the classical $3.17U_p$ trend, whereas under BSV light, the returning electron current remains predominantly concentrated in the low-velocity region. Relative to figure 2(b), the distribution in figure 6(b) extends slightly further toward higher velocities, consistent with the weak high-velocity tail of the returning current observed at large $|x|$ in figure 4(d). These results demonstrate that the pronounced low-velocity concentration of the returning electron current under BSV light is robust against moderate variations in the VD position.

The second remark concerns the relationship between the reconstructed trajectories and the driving-field properties. Under coherent light, the electron motion is mainly governed by the expectation value of the field operator, leading to regular, field-driven trajectories that closely resemble the motion expected under classical-field driving. In contrast, for BSV light, the expectation value of the field operator vanishes, and the driving effect is dominated by electric-field fluctuations. The resulting trajectories are therefore dispersed and desynchronized, rather than organized into coordinated motion by a deterministic field. Thus, the reconstructed trajectories reflect part of the electron dynamical information shaped by the properties of the driving field.

The third remark concerns recollision dynamics driven by a squeezed coherent state. As shown in figures 7(a)–(c), the bound trajectories remain localized near the ionic core and exhibit regular oscillations, while the unbound trajectories show large-amplitude excursions on both sides of the core. Compared with the coherent-light case, however, the returning part of the unbound trajectories becomes less concentrated and less prominent in the trajectory ensemble. This tendency is also reflected in the phase-space distributions in figures 7(d) and (e). In particular, the unbound-trajectory distribution in figure 7(e) shows a clear asymmetry between outgoing and returning motion, with the returning branch reaching a smaller velocity extent than the outgoing branch. Therefore, the squeezed coherent state exhibits an intermediate behavior: it retains more organized oscillatory motion than BSV light, while the squeezing-induced fluctuations already weaken the coordinated high-velocity return found under coherent driving.

The fourth remark concerns the applicability of the recollision picture and the conventional induced-dipole HHG calculation under quantum-light driving. Under coherent light, the nonzero field expectation value provides an average electric field with a well-defined amplitude and phase, which supports synchronized return motion. At the same time, the induced atomic dipole is nonzero, and its Fourier

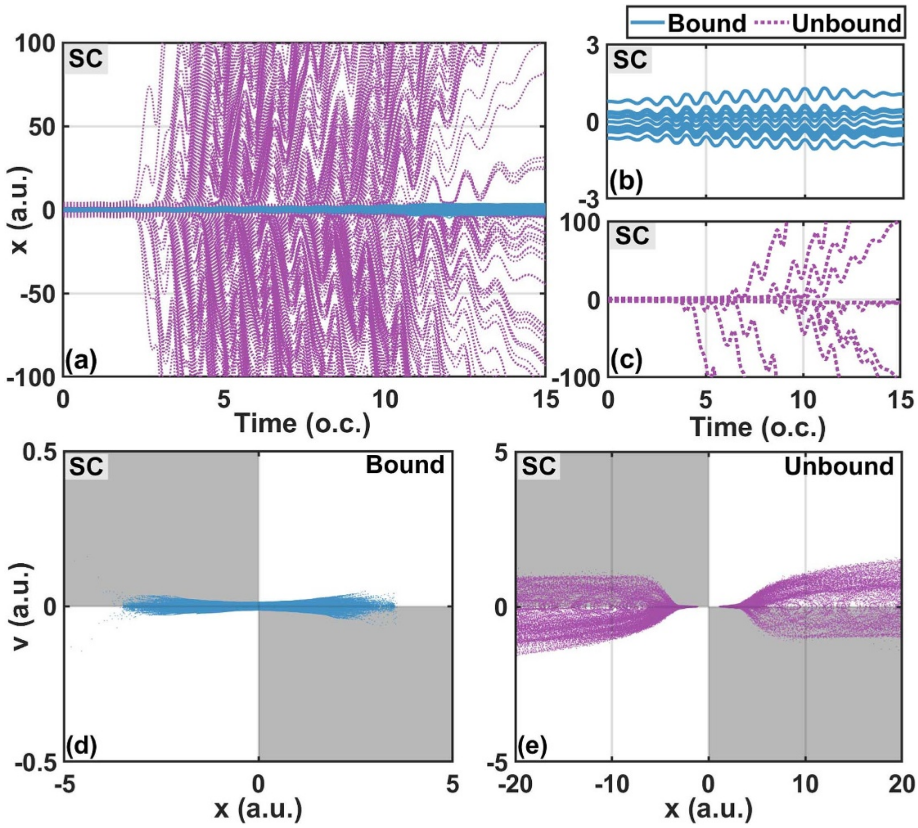

Figure 7. Recollision dynamics driven by a squeezed coherent state. (a) Reconstructed electron trajectories. (b) and (c) show selected bound- and unbound-electron trajectories, respectively. (d) and (e) show velocity-position phase-space distributions for bound- and unbound-electron trajectories, respectively. The average light intensity is 3×10^{14} W cm^{-2}, and the squeezing-induced photon number is twice the coherent-component photon number.

spectrum is connected to the classical cutoff law through the recollision picture. Under BSV light, however, the field expectation value vanishes and the induced atomic dipole is zero, while strong electric-field fluctuations do not support the same synchronized return motion [27]. Consequently, the conventional induced-dipole calculation cannot account for BSV-driven HHG, and a classical-trajectory recollision scenario is insufficient for describing its mechanism. This calls for caution when extending coherent-light physical pictures to noncoherent light fields with pronounced quantum features, where the underlying mechanisms may go beyond semiclassical descriptions [30].

5. Conclusion

In this work, we have investigated electron dynamics driven by coherent light and BSV light using the VD method. By tracking the probability current, we extracted local velocity distributions of the returning electron current and reconstructed global probability-flow trajectories, thereby characterizing the dynamics from both local and global perspectives. Whereas coherent light produces the well-known organized return dynamics associated with the recollision picture, BSV light gives rise to qualitatively different behavior, characterized by strongly suppressed returning-current velocities, dispersed probability-flow trajectories, and the absence of coordinated return motion. Despite the generation of high-order harmonics, the conventional recollision picture no longer provides a direct dynamical description of the strong-field response driven by BSV light.

More broadly, our results demonstrate that strong-field phenomena induced by noncoherent quantum light can be governed by dynamical mechanisms fundamentally different from those established for coherent driving fields. These findings highlight the limitations of directly extending the conventional coherent-field recollision picture to BSV-driven strong-field dynamics. At the same time, the VD-based probability-current analysis developed here provides a versatile framework for probing electron dynamics beyond the classical-field paradigm and may prove valuable for future studies of strong-field interactions driven by nonclassical light.

Acknowledgement

This work was supported by NSFC Grant Nos. 12474484, 12688201, 12274384, and 12450404.

Data availability statement

The data that support the findings of this study are openly available at the following URL/DOI: https://doi.org/10.6084/m9.figshare.32617071 [74].

ORCID iDs

Haoyu Liu 0009-0000-5985-0163
Jianmin Yuan 0000-0002-9315-0854
Xu Wang 0000-0002-8043-7135

References

[1] Kulander K C, Schafer K J and Krause J L 1993 Dynamics of short-pulse excitation, ionization and harmonic conversion *Super-Intense Laser-Atom Physics* (Springer) p 95
[2] Schafer K J, Yang B, DiMauro L F and Kulander K C 1993 Above threshold ionization beyond the high harmonic cutoff *Phys. Rev. Lett.* **70** 1599
[3] Corkum P B 1993 Plasma perspective on strong field multiphoton ionization *Phys. Rev. Lett.* **71** 1994
[4] McPherson A, Gibson G, Jara H, Johann U, Luk T S, McIntyre I, Boyer K and Rhodes C K 1987 Studies of multiphoton production of vacuum-ultraviolet radiation in the rare gases *J. Opt. Soc. Am. B* **4** 595
[5] Ferray M, L'Huillier A, Li X F, Lompré L A, Mainfray G and Manus C 1988 Multiple-harmonic conversion of 1064 nm radiation in rare gases *J. Phys. B: At. Mol. Opt. Phys.* **21** L31
[6] Paul P M, Toma E S, Breger P, Mullot G, Augé F, Balcou P, Muller H G and Agostini P 2001 Observation of a train of attosecond pulses from high harmonic generation *Science* **292** 1689
[7] Hentschel M, Kienberger R, Spielmann C, Reider G A, Milosevic N, Brabec T, Corkum P, Heinzmann U, Drescher M and Krausz F 2001 Attosecond metrology *Nature* **414** 509
[8] Fittinghoff D N, Bolton P R, Chang B and Kulander K C 1992 Observation of nonsequential double ionization of helium with optical tunneling *Phys. Rev. Lett.* **69** 2642
[9] Walker B, Sheehy B, DiMauro L F, Agostini P, Schafer K J and Kulander K C 1994 Precision measurement of strong field double ionization of helium *Phys. Rev. Lett.* **73** 1227
[10] Staudte A *et al* 2007 Binary and recoil collisions in strong field double ionization of helium *Phys. Rev. Lett.* **99** 263002
[11] Ye D F, Liu X and Liu J 2008 Classical trajectory diagnosis of a finger like pattern in the correlated electron momentum distribution in strong field double ionization of helium *Phys. Rev. Lett.* **101** 233003
[12] Becker W, Liu X, Ho P J and Eberly J H 2012 Theories of photoelectron correlation in laser-driven multiple atomic ionization *Rev. Mod. Phys.* **84** 1011
[13] Morishita T, Le A T, Chen Z and Lin C D 2008 Accurate retrieval of structural information from laser-induced photoelectron and high-order harmonic spectra by few-cycle laser pulses *Phys. Rev. Lett.* **100** 013903
[14] Blaga C I, Xu J, DiChiara A D, Sistrunk E, Zhang K, Agostini P, Miller T A, DiMauro L F and Lin C D 2012 Imaging ultrafast molecular dynamics with laser-induced electron diffraction *Nature* **483** 194
[15] Wolter B *et al* 2016 Ultrafast electron diffraction imaging of bond breaking in di-ionized acetylene *Science* **354** 308
[16] Wang W, Zhou J, Liu B and Wang X 2021 Exciting the isomeric Th 229 nuclear state via laser-driven electron recollision *Phys. Rev. Lett.* **127** 052501
[17] Wang X 2022 Nuclear excitation of Th 229 induced by laser-driven electron recollision *Phys. Rev. C* **106** 024606
[18] Iskhakov T, Pérez A M, Spasibko K, Chekhova M V and Leuchs G 2012 Superbunched bright squeezed vacuum state *Opt. Lett.* **37** 1919
[19] Spasibko K, Kopylov D, Krutyanskiy V, Murzina T, Leuchs G and Chekhova M 2017 Multiphoton effects enhanced due to ultrafast photon-number fluctuations *Phys. Rev. Lett.* **119** 223603
[20] Manceau M, Spasibko K, Leuchs G, Filip R and Chekhova M 2019 Indefinite-mean Pareto photon distribution from amplified quantum noise *Phys. Rev. Lett.* **123** 123606
[21] Rasputnyi A, Chen Z, Birk M, Cohen O, Kaminer I, Krüger M, Seletskiy D, Chekhova M and Tani F 2024 High-harmonic generation by a bright squeezed vacuum *Nat. Phys.* **20** 1960
[22] Lemieux S, Jalil S A, Purschke D N, Boroumand N, Hammond T J, Villeneuve D, Naumov A, Brabec T and Vampa G 2025 Photon bunching in high-harmonic emission controlled by quantum light *Nat. Photon.* **19** 767
[23] Tzur M E *et al* 2025 Attosecond-resolved quantum fluctuations of light and matter (arXiv:2511.18362)
[24] Heimerl J, Mikhaylov A, Meier S, Höllerer H, Kaminer I, Chekhova M and Hommelhoff P 2024 Multiphoton electron emission with non-classical light *Nat. Phys.* **20** 945
[25] Heimerl J, Rasputnyi A, Pölloth J, Meier S, Chekhova M and Hommelhoff P 2025 Quantum light drives electrons strongly at metal needle tips *Nat. Phys.* **21** 1899
[26] Jiang Z *et al* 2026 Nonlinear atomic tunnelling boosted by bright squeezed vacuum *Nature* **654** 356–60
[27] Gorlach A, Tzur M E, Birk M, Krüger M, Rivera N, Cohen O and Kaminer I 2023 High-harmonic generation driven by quantum light *Nat. Phys.* **19** 1689
[28] Tzur M E, Birk M, Gorlach A, Kaminer I, Krüger M and Cohen O 2024 Generation of squeezed high-order harmonics *Phys. Rev. Res.* **6** 033079

[29] Gothelf R V, Lange C S and Madsen L B 2025 High-order harmonic generation in a crystal driven by quantum light *Phys. Rev. A* **111** 063105
[30] Liu H, Zhang H, Wang X and Yuan J 2026 Theory of high harmonic generation with quantum light *Phys. Rev. Res.* **8** 023326
[31] Wang S and Lai X 2023 High-order above-threshold ionization of an atom in intense quantum light *Phys. Rev. A* **108** 063101
[32] Lyu Z, Sun F, Fang Y, He Q and Liu Y 2025 Effect of photon quantum statistics on electrons in above-threshold ionization *Phys. Rev. Res.* **7** L012072
[33] Liu H, Zhang H, Wang X and Yuan J 2025 Atomic double ionization with quantum light *Phys. Rev. Lett.* **134** 123202
[34] Piazza A D and Qu K 2026 Control of nonlinear Compton scattering in a squeezed vacuum *Phys. Rev. Lett.* **136** 085001
[35] Tzur M E, Birk M, Gorlach A, Krüger M, Kaminer I and Cohen O 2023 Photon-statistics force in ultrafast electron dynamics *Nat. Photon.* **17** 501
[36] Fang Y, Sun F X, He Q and Liu Y 2023 Strong-field ionization of hydrogen atoms with quantum light *Phys. Rev. Lett.* **130** 253201
[37] Rivera-Dean J, Stammer P, Ciappina M and Lewenstein M 2025 Structured squeezed light allows for high-harmonic generation in classical forbidden geometries *Phys. Rev. Lett.* **135** 013801
[38] Tzur M E and Cohen O 2024 Motion of charged particles in bright squeezed vacuum *Light Sci. Appl.* **13** 41
[39] Feuerstein B and Thumm U 2003 On the computation of momentum distributions within wavepacket propagation calculations *J. Phys. B* **36** 707
[40] Wang X, Tian J and Eberly J 2013 Extended virtual detector theory for strong-field atomic ionization *Phys. Rev. Lett.* **110** 243001
[41] Teeny N, Keitel C H and Bauke H 2016 Virtual-detector approach to tunnel ionization and tunneling times *Phys. Rev. A* **94** 022104
[42] Wang X, Tian J and Eberly J H 2018 Virtual detector theory for strong-field atomic ionization *J. Phys. B: At. Mol. Opt. Phys.* **51** 084002
[43] Xu R and Wang X 2021 Extended virtual detector theory including quantum interferences *AIP Adv.* **11** 025124
[44] Younis D and Eberly J H 2023 Strong-field nonsequential double photoionization using virtual-detector theory with path summation *Phys. Rev. A* **107** 053117
[45] Wyatt R E 2005 *Quantum Dynamics With Trajectories: Introduction to Quantum Hydrodynamics* (Springer)
[46] Bohm D 1952 A suggested interpretation of the quantum theory in terms of 'hidden' variables *I Phys. Rev.* **85** 166
[47] Sanz A S and Miret-Artés S 2012 *A Trajectory Description of Quantum Processes. I. Fundamentals: A Bohmian Perspective* vol 850 (Springer)
[48] Lai X-Y and Liu X-J 2020 Bohmian trajectory perspective on strong field atomic processes *Chin. Phys. B* **29** 013205
[49] Boykin T B, Luisier M and Klimeck G 2010 Current density and continuity in discretized models *Eur. J. Phys.* **31** 1077
[50] Kocsis S, Braverman B, Ravets S, Stevens M J, Mirin R P, Shalm L K and Steinberg A M 2011 Observing the average trajectories of single photons in a two-slit interferometer *Science* **332** 1170
[51] Luis A and Sanz A S 2015 What dynamics can be expected for mixed states in two-slit experiments? *Ann. Phys.* **357** 95
[52] Teeny N, Yakaboylu E, Bauke H and Keitel C H 2016 Ionization time and exit momentum in strong-field tunnel ionization *Phys. Rev. Lett.* **116** 063003
[53] Ni H, Saalmann U and Rost J-M 2016 Tunneling ionization time resolved by backpropagation *Phys. Rev. Lett.* **117** 023002
[54] Tian J, Wang X and Eberly J H 2017 Numerical detector theory for the longitudinal momentum distribution of the electron in strong field ionization *Phys. Rev. Lett.* **118** 213201
[55] Javanainen J, Eberly J H and Su Q 1988 Numerical simulations of multiphoton ionization and above-threshold electron spectra *Phys. Rev. A* **38** 3430
[56] Su Q and Eberly J H 1991 Model atom for multiphoton physics *Phys. Rev. A* **44** 5997
[57] Scully M O and Zubairy M S 1997 *Quantum Optics* (Cambridge University Press)
[58] Grynberg G, Aspect A and Fabre C 2010 *Introduction to Quantum Optics: From the Semi-Classical Approach to Quantized Light* (Cambridge University Press)
[59] Gerry C C and Knight P L 2023 *Introductory Quantum Optics* (Cambridge University Press)
[60] Carmichael H J 2013 *Statistical Methods in Quantum Optics 1: Master Equations and Fokker-Planck Equations* (Springer)
[61] Das S and Green J R 2022 Density matrix formulation of dynamical systems *Phys. Rev. E* **106** 054135
[62] Mousavi S V and Miret-Artés S 2023 Quantum classical transition for mixed states: the scaled Von Neumann equation *Symmetry* **15** 1184
[63] Sanz A S and Borondo F 2007 A quantum trajectory description of decoherence *Eur. Phys. J. D* **44** 319
[64] Cohen-Tannoudji C, Diu B and Laloe F 1977 *Quantum Mechanics* (Hermann and Wiley)
[65] Sanz A S and Borondo F 2009 Contextuality, decoherence and quantum trajectories *Chem. Phys. Lett.* **478** 301
[66] Tsatrafyllis N *et al* 2019 Quantum optical signatures in a strong laser pulse after interaction with semiconductors *Phys. Rev. Lett.* **122** 193602
[67] de-la-Pena S, Neufeld O, Even Tzur M, Cohen O, Appel H and Rubio A 2024 Quantum electrodynamics in high-harmonic generation: multitrajectory Ehrenfest and exact quantum analysis *J. Chem. Theory Comput.* **21** 283
[68] Casella G and Berger R 2024 *Statistical Inference* (Chapman and Hall/CRC)
[69] Devroye L 2006 Nonuniform random variate generation *Handb. Oper. Res. Manag. Sci.* **13** 83
[70] Hammersley J 2013 *Monte Carlo Methods* (Springer)
[71] Song Y, Guo F-M, Li S-Y, Chen J-G, Zeng S-L and Yang Y-J 2012 Investigation of the generation of high-order harmonics through Bohmian trajectories *Phys. Rev. A* **86** 033424
[72] Wu J, Augstein B B and Figueira de Morisson Faria C 2013 Local dynamics in high-order-harmonic generation using Bohmian trajectories *Phys. Rev. A* **88** 023415
[73] Wu J, Augstein B B and Figueira de Morisson Faria C 2013 Bohmian-trajectory analysis of high-order-harmonic generation: ensemble averages, nonlocality and quantitative aspects *Phys. Rev. A* **88** 063416
[74] Haoyu L 2026 Electron recollision with bright squeezed vacuum light *Figshare* (https://doi.org/10.6084/m9.figshare.32617071)